Colloids and Surfaces A: Physicochemical and Engineering Aspects 753 (2027) 142043

Contents lists available at ScienceDirect

Colloids and Surfaces A: Physicochemical and Engineering Aspects

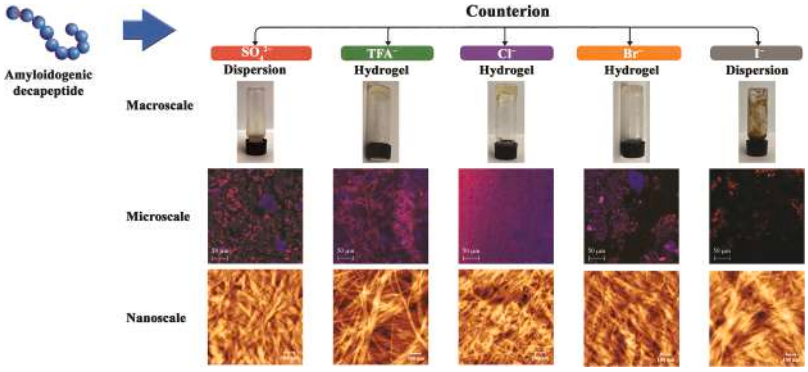
journal homepage: www.elsevier.com/locate/colsurfa

Counterion effects on the amyloid morphology of a peptide gel

Mert Acar [a], Duccio Tatini [b], Ilaria Clemente [b], Luigi Talarico [b], Agnese Magnani [b], Michael Quagliata [a,c], Francesca Nuti [a,c], Anna Maria Papini [a,c], Pierandrea Lo Nostro [a,*]

[a] Department of Chemistry "Ugo Schiff", University of Florence, Sesto Fiorentino, 50019, Italy
[b] Department of Biotechnologies, Chemistry and Pharmacy, University of Siena, Siena, 53100, Italy
[c] PeptLab, University of Florence, Sesto Fiorentino, 50019, Italy

GRAPHICAL ABSTRACT



ARTICLE INFO

Keywords:
Peptide gels
Amyloids
Morphology
Specific ion effects
Hydrogels

ABSTRACT

In this study we investigated amyloid hydrogels produced by a decapeptide fragment of the acyl carrier protein (ACP) in water, in the presence of different counterions: trifluoroacetate (TFA^-), SO_4^{2-}, Cl^-, Br^-, and I^-, through confocal laser scanning microscopy (CLSM), atomic force microscopy (AFM), attenuated total reflectance Fourier-transform infrared spectroscopy (ATR-FTIR), circular dichroism (CD), fluorescence spectroscopy, rheological measurements, to understand how the nature of the counterion affects amyloid morphology across length scales, secondary structure, and the mechanical response of the gels. The results show that the nature of the counterion profoundly affects the gelation properties, amyloid morphology, and rheological properties. The results bear an important implication on the choice of post-synthesis counterion to accommodate a correct modeling of the system of interest.

1. Introduction

Amyloids are a class of fibrous protein aggregates that play a pivotal role in various pathological conditions, including neurodegenerative disorders such as Parkinson's and Alzheimer's diseases [1–7]. Although amyloid structures have long been a subject of research and the

* Corresponding author.
E-mail address: pierandrea.lonostro@unifi.it (P. Lo Nostro).

https://doi.org/10.1016/j.colsurfa.2026.142043
Received 16 July 2026; Received in revised form 21 September 2026; Accepted 7 October 2026
Available online 8 October 2026
0927-7757/© 2026 Published by Elsevier B.V.

understanding of these structures has greatly advanced, significant gaps in our knowledge remain [1,4–7].

The pathological conditions are due to the misfolding of native proteins, where the unfolded polypeptide chains can assemble into different oligomeric states [8,9] These oligomers can either remain as off-pathway species or progress towards the formation of amyloid fibrils, i.e. on-pathway route [9,10]. While the initial nucleation of amyloid fibrils is a slow process, the following elongation occurs at an exponential rate [8–10]. The resulting elongated structures then adopt the characteristic cross-β sheet conformation that defines amyloid fibrils [8–10], which can further associate, either with themselves or with other biomacromolecules, to generate higher-order amyloid aggregates, the so-called *plaques* [10,11].

The aggregates comprise a complex mixture of various morphological states, including oligomers, protofibrils, and fibrils with distinct conformations [10]. Amyloid fibrils exhibit a remarkable variety of nanoassemblies as shown by their structural polymorphism, with differences in twist, curvature, and packing arrangements, despite the common cross-β sheet core [10].

They also possess remarkable material properties. They can form multi-responsive gels [12–14] and can be exploited in cell culture [15,16], drug delivery [15,17], tissue engineering [15], and as sensors [18,19]. Although uncertainties remain about their safety and toxicity [20–22], these studies provide valuable insights into the amyloid formation, behavior, and morphology.

To this end, solid-phase peptide synthesis (SPPS) is an important tool in amyloid research and the development of functional materials [23–27]. SPPS leads to the synthesis of peptides that mimic the properties of natural amyloids, providing valuable insights into amyloid self-assembly and fibrillization mechanisms [14,18,19]. Moreover, SPPS promoted the development of novel peptide-based materials with controlled structures and properties by incorporating amyloidogenic sequences or motifs into peptide designs [14,28–30].

However, a frequently overlooked aspect of SPPS is the presence of counterions and their chemical nature, which can significantly impact the system properties. Trifluoroacetic acid (TFA) is a reagent used in SPPS; therefore, synthetic peptides are often isolated after lyophilization, at least in part, as TFA^- salts. Even after multiple lyophilization cycles, the final product retains the tightly bound TFA^- counterions due to strong ion pairing with positively charged peptide groups and the protonated free N-terminus [31–34]. This effect is especially pronounced when the peptide sequence contains many positively charged residues, such as Arg, Lys, and His.

Although purification strategies exist to reduce TFA concentration, such as repeated lyophilization from dilute HCl, exchange on ion-exchange resins, and RP-HPLC with volatile acids, these can only replace TFA^- with different counterions [31–34], depending on the peptide sequence.

This raises the question of whether the counterion nature may influence the overall behavior and properties of the systems under investigation, as they can create a microenvironment that influences peptide conformation, aggregation, and biological activity.

Specific ion (Hofmeister) effects may cause deviations in the physicochemical properties of solutions and dispersions, depending on the nature and concentration of the intervening species [35,36]. Typically at salt concentrations higher than 0.17 M electrostatic interactions vanish and ion-specific non-electrostatic forces between the different components of the system (aggregates, solvent and solutes) become significant [35,36] and emerge in a variety of interesting phenomena [37–40].

Specific ion effects are observed in various systems and are of utmost importance in both chemistry, biology, and formulation applications [35,41–44]. These effects depend on the nature of the ions and arise from a combination of underlying mechanisms [35,41–46].

In a previous study we extensively investigated the properties of 3% w/v ACP(65−74)-NH_2 amyloid gels in different solvents [14]. Here, we studied the 3% w/v hydrogels of ACP(65−74)-NH_2 in the presence of various counterions: TFA^-, SO_4^{2-}, Cl^-, Br^-, and I^-. The C-terminus was left in its amidated form to allow comparison with previous results [14]. The system contained no background added salt. The counterions came directly from the original synthetic procedure (TFA^-), post-lyophilization, or from ion-exchange, where TFA^- was replaced by the conjugate bases of strong acids.

The scope of this paper is to study how Hofmeister effects shape the macro- and microscopic properties, morphology, and rheological behavior of this hydrogel. Here we use *"Hofmeister effects"* and *"specific ion effects"* interchangeably and refer to an entire class of ion-specific phenomena that depend on the specific chemical nature of the ion, including its polarizability, hydration, and ion-pairing energy, and not only its charge and concentration. In particular, we address three relevant questions related to the formation of amyloid structures: i) how do these counterions affect the self-assembly and morphology of the amyloid fibrils and aggregates? ii) do these ion effects provide a better understanding of the formation of amyloids? iii) are these synthetic amyloid models really representative for natural systems?

To achieve this, we use multiple complementary techniques, including confocal laser scanning microscopy (CLSM), atomic force microscopy (AFM), attenuated total reflectance Fourier-transform infrared spectroscopy (ATR-FTIR), circular dichroism (CD), fluorescence spectroscopy, rheological measurements, and we interpret the results through the lens of Hofmeister series to understand how the nature of the counterion affects amyloid morphology across length scales, secondary structure, and the mechanical response of the gels.

2. Experimental section

2.1. Chemicals

Peptide-synthesis grade acetonitrile (ACN) (99.95%) and N,N-dimethylformamide (DMF) (99.8%) were purchased from Carlo Erba (Milano, Italy). Triisopropyl silane (TIS) (>98%) and diethyl ether (>99%) were purchased from Sigma Aldrich (Milano, Italy). Rink Amide AM resin (0.67 mmol/g), Fmoc amino acids (>98%), DIC (>99%), Oxyma Pure (>99%) were purchased from Novabiochem (Merck KGaA, Darmstadt, Germany). Ethyl acetate (EtOAc) (99%), dimethylsulfoxide (DMSO) (98.5%), trifluoroacetic acid (TFA) (99%), NaH_2PO_4 (>99%), Na_2HPO_4 (>99%), Na_2CO_3 (>99%), NaOH (≥97%), HCl (37%), H_2SO_4 (99.9%), HBr (48%), HI (57%), Thioflavin T (dye content ≥65%), and Rhodamine B isothiocyanate (labelling efficiency with bovine albumin >70%) were acquired from Sigma-Aldrich (Milan, Italy).

Bidistilled Milli-Q water with a resistivity > 18 MΩ•cm and a conductivity of 0.055 $\mu S \bullet cm^{-1}$ at 25°C was used throughout the experiments.

2.2. Synthesis and determination of Trifluoroacetic Acid (TFA)

The ACP(65−74)-NH_2 (VQAAIDYING-NH_2) peptide was synthesized following the previously established protocols using the Fmoc/tBu strategy on 1 mmol scale with the PurePep Chorus synthesizer (Gyros Protein Technologies, AZ, USA), taking advantage of magnetic induction heating [14]. For the washing steps, an eco-friendly binary solvent mixture of ethyl acetate and dimethyl sulfoxide (8:2 v/v) was employed. The Fmoc deprotection was performed with a 20% (v/v) piperidine solution in DMF at 90° C for 1 min. The coupling reactions were conducted using a mixture containing Fmoc-amino acid, diisopropylcarbodiimide (DIC), and Oxyma Pure, with reaction conditions set to 90 °C for 2 min. Cleavage from the resin, along with simultaneous removal of all sidechain protecting groups, was achieved using a cocktail comprising trifluoroacetic acid, triisopropylsilane, and water (95:2.5:2.5 v/v/v) at room temperature over 2.5 h. The cleaved product was then precipitated from the TFA solution using cold diisopropyl ether at 0 °C.

The crude peptide was then purified by flash chromatography, and fractions with a purity exceeding 95% (determined as the percentage of

the target peak area relative to the total chromatographic area) were collected.

TFA^- counterions accounted for 2.1% w/w of the purified peptide. For the exchange of counterion, ACP(65−74)-NH_2 (0.75 mmol, 1eq) was dissolved in H_2O:ACN 2:1 (20 mL). The mineral acids (2eq) were added to the solutions. In particular, 113 μL of HCl (37% (w/v) in H_2O), 170 μL of HBr (48% (w/v) in H_2O), 198 μL of HI (57% (w/v) in H_2O) and 80 μL of H_2SO_4. Then the mixtures were lyophilized. This procedure was performed twice to obtain ACP(65−74)-NH_2•HCl, ACP(65−74)-NH_2•HBr, ACP(65−74)-NH_2•HI and ACP(65−74)-NH_2•H_2SO_4.

After the counterion exchange, the trifluoroacetic acid (TFA) presence was checked using the standard protocol from Waters [47] by Ultra-performance liquid chromatography (UPLC; ACQUITY UPLC, Waters, Milford, MA, USA) coupled with a Waters Xevo TQ-S triple quadrupole mass spectrometer equipped with an electrospray ionization (ESI) source. Chromatographic separation was performed using an Atlantis™ Premier BEH C18 AX column (1.7 μm, 2.1 × 100 mm; Waters, Milford, MA, USA). The column and the sample were kept at 60 °C and 15 °C, respectively. The flow rate was 0.500 mL/min, and the injection volume was 20 μL. The mobile phase was 2 mM ammonium acetate with 0.001% formic acid. Highly aqueous isocratic conditions were employed, with a retention time (t_R) of 2.51 min for TFA.

Mass spectrometric detection was performed in negative electrospray ionization mode. Two multiple reaction monitoring (MRM) transitions were monitored for TFA: m/z 112.9 > 68.9 for quantification (QN) and m/z 112.9 > 112.9 for confirmation (QL). Calibration curves showed coefficients of determination (R^2) > 0.997 using a 1/x linear regression model. Blanks, calibration standards, and samples were prepared in polypropylene injection vials using Milli-Q ultrapure water. Calibration standards covered the concentration range of 10–25,000 ng/mL (see Figure S1 in Supplementary Material). Data acquisition and processing were performed using the MassLynx™ software, version 4.2 (Waters, Milford, MA, USA), including TargetLynx XS version 4.2.

Following the exchange procedure, TFA concentrations were below the limit of quantification (LOQ) (<10 ng/mL, < 0.08 μM) in all analyzed samples, demonstrating the effective removal of TFA from the peptide preparation.

The resulting counterion fractions were 2.1% TFA^-, 0.65% Cl^-, 1.5% Br^-, 2.3% I^- and 1.8% SO_4^{2-} (w/w). Peptide contents were therefore 97.9, 99.4, 98.5, 97.7 and 98.2% w/w, respectively.

2.3. Sample preparation

3% w/v ACP(65−74)-NH_2, with each sample containing a different counterion, was dissolved in water at 25 °C. For each preparation the weighed powder mass was corrected for its counterion fraction, so that all five samples contained 28 mM peptide and 5.6 mM anion. The samples were magnetically stirred until complete dispersion and then allowed to rest for 24 h before testing. The sample pH was not adjusted, except for the pH responsiveness studies, and all resulting gels had a pH of 3.

2.4. pH responsiveness

To investigate the pH responsiveness of the samples, NaOH was added to reach a pH of 10 or higher. To test the reversibility, HCl was then used to revert to the initial pH. During the addition of NaOH and HCl, the concentrations were carefully controlled to prevent dilution effects.

Additionally, 10 mM aqueous buffers with 3% w/v peptide were prepared at four distinct pH values: 3, 7, 10, and 12 as shown in the Table S1 (Supplementary Material).

2.5. Confocal laser scanning microscopy (CLSM)

Confocal images of samples stained with 8 μM Rhodamine B isothiocyanate (RBITC) and 8 μM Thioflavin T (ThT) were acquired using a TCS SP8 Confocal Microscope (Leica Microsystems GmbH, Wetzlar, Germany) equipped with a 20X/0.75 dry objective (Zeiss), an Argon ion laser for excitation (λ = 458 and 516 nm), and two PMT detectors (selected detection range 480–500 and 580–600 nm). The pinhole was set to 1.0 Airy unit. The images were acquired at 512 × 512 pixels and 8-bit depth with unidirectional scanning at 400 Hz and zoom 1.875, yielding a lateral pixel size of 0.606 μm across a 310 × 310 μm field. Z-stacks were acquired along the galvanometric z-axis at the system-optimized step size of 0.685 μm. Lab-Tek Chambers with borosilicate glass coverslips were used as sample holder. Images were acquired from three independent preparations per sample, and ten fields were examined per preparation.

2.6. Atomic force microscopy (AFM)

Images were acquired in tapping mode using a NX7 atomic force microscope (Park Systems, Suwon, Republic of Korea) equipped with a cantilever tip SCOUT-350 RAI (Nu Nano, Bristol, UK), with 350 kHz frequency, 5 nm nominal tip radius and 42 N/m nominal spring constant. The doped silicon cantilever was Al-coated on detector side to enhance laser beam reflectivity. The scan areas were 1 × 1 μm at a resolution of 1024 × 1024 pixels at a scan rate of 0.60 Hz.

The samples were deposited on a freshly cleaved mica surface and left to dry. Obtained images were processed using the Gwyddion [48,49]. Trace_y software [50–52] was used to trace and digitally straighten individual fibrils from AFM images, and to extract parameters including helical pitch, minimum, maximum, and mean heights, cross-sectional profiles, from which a 3D model was reconstructed.

2.7. Fourier-transform infrared spectroscopy (FTIR)

FTIR spectra of all samples were recorded in Attenuated Total Reflection (ATR) mode using a Thermo Nicolet Nexus 870 (Thermo Electron Corp, Madison, USA) with an MCT detector. Spectra were acquired between 650 cm^{-1} and 4000 cm^{-1} with a spectral resolution of 2 cm^{-1} and 128 scans per spectrum. Chamber baseline correction was applied to each spectrum. Possible interference of the TFA band with the *Amide I* region was excluded by a reference spectrum of TFA in water at the same concentration as in the sample (see Figure S2 in the Supplementary Material). Standard normal variate (SNV) normalization and offset normalization were also applied to remove multiplicative scatter effects, standardize spectral data and correct for baseline shifts, ensuring a minimum absorbance of zero. The normalized reference spectrum (Milli-Q water) was subtracted from each spectrum. An eleven-point Savitzky-Golay function with a polynomial order of 2 was used to smooth the spectra. The spectra were truncated to the 1700–1600 cm^{-1} range (Amide I region) and a linear baseline correction was applied. Each spectrum was normalized to the maximum absorbance of the Amide I band. The spectra were then deconvoluted and fitted using Gaussian curves and a constant baseline. The initial number of peaks and their positions were chosen based on the second-derivative spectra. First, the positions and widths were held, and the height was fitted with constraints between 0 and 1. Then the width was allowed to change, constrained between 0 and 25. Finally, a final fit was made without constraints, and the procedure was optimized until a residual lower than ± 0.02 was obtained. The secondary structure percentages were obtained from three independent preparations of the same sample, each fitted with the identical procedure, and have an uncertainty of ± 5%. The resultant deconvoluted bands of Amide I were assigned to different secondary protein structures [53–58].

2.8. Circular dichroism

Circular dichroism (CD) spectra were recorded with a J-715 spectropolarimeter (JASCO, Tokyo, Japan) at a scan speed of 20 nm/min.

Data were collected from 190 to 250 nm at 25 °C using 1 mm Hellma quartz cuvettes (Hellma, Muellheim, Germany). Samples included aqueous dispersions of ACP(65−74)-NH_2 at 0.01% w/v concentration in the presence of different counterions. Each spectrum was an accumulation of five spectra, after subtracting the water signal subtracted. Ellipticity values were converted to delta epsilon ($\Delta\varepsilon$) to account for concentration during deconvolution, which was performed using the BeStSel server [59,60]. All fittings achieved a normalized root-mean-square deviation (NRMSD) value below 0.04, indicating an acceptable fit.

2.9. Fluorescence spectroscopy

Fluorescence measurements were conducted at 25 °C in 1 cm pathlength quartz cuvettes (Hellma, Muellheim, Germany) using a LS50B spectrofluorometer (Perkin-Elmer, Cambridgeshire, UK) equipped with a Haake thermostat. The experiments were carried out on ACP(65−74)-NH_2 aqueous dispersions at 0.01% w/v with different counterions in the presence of 0.3 μM Thioflavin T (ThT) to monitor the presence of amyloids. Emission spectra were recorded from 450 to 600 nm with a 440 nm excitation wavelength, at a scan speed of 100 nm/min and 15 × 15 nm slit widths for both the excitation and emission. Each spectrum was an accumulation of five spectra. The spectrum of 0.01% w/v peptide fragment without ThT was subtracted from each of the spectrum.

2.10. Rheology

Frequency sweep tests were carried out using a Discovery Hybrid Rheometer HR3 (TA Instruments, New Castle, Delaware, USA) equipped with a cone-plate geometry (40 mm diameter, 2° angle) at 25 °C. The experiments were performed in controlled shear-stress mode, with a Peltier system for temperature regulation. Amplitude sweep tests were used to identify the Linear Viscoelastic Region (LVER) (see Figure S3 in the Supplementary Material) and to select the strain amplitudes employed in the oscillatory experiments. A 1% strain was set for the frequency sweeps, where the storage (G') and loss (G'') moduli were measured across a frequency range of 10^{-3} to 10^{2} Hz setting a strain of 1% for all the samples. Silicone oil was applied to the sample edges to minimize solvent evaporation during testing [61].

To evaluate the gel recovery after shear deformation, three-interval thixotropy tests (3ITT) were performed. In the first interval a small strain within the LVER (0.1%) is applied over time. In the second interval, the strain is increased to 50% (beyond the LVER) to disrupt the gel structure. During the third interval, the strain is reduced back to 0.1%, and gel recovery is monitored. The oscillation frequency is kept constant at 1.0 Hz during the three steps. The detailed experimental procedure is reported in our previous work [14]. The Recovery Ratio (RR) was calculated using Eq. 1:

$$RR = \frac{G'_{60s}}{G'_{initial}} \bullet 100 \quad (1)$$

where $G'_{initial}$ refers to the storage modulus during the first interval, and $G'_{60\,s}$ corresponds to the modulus after 60 s in the third interval. All rheological tests were performed in triplicate.

3. Results and discussion

3.1. Macroscopic appearance and pH responsiveness

Fig. 1 shows 3% w/v ACP(65−74)-NH_2 samples in water at 25 °C

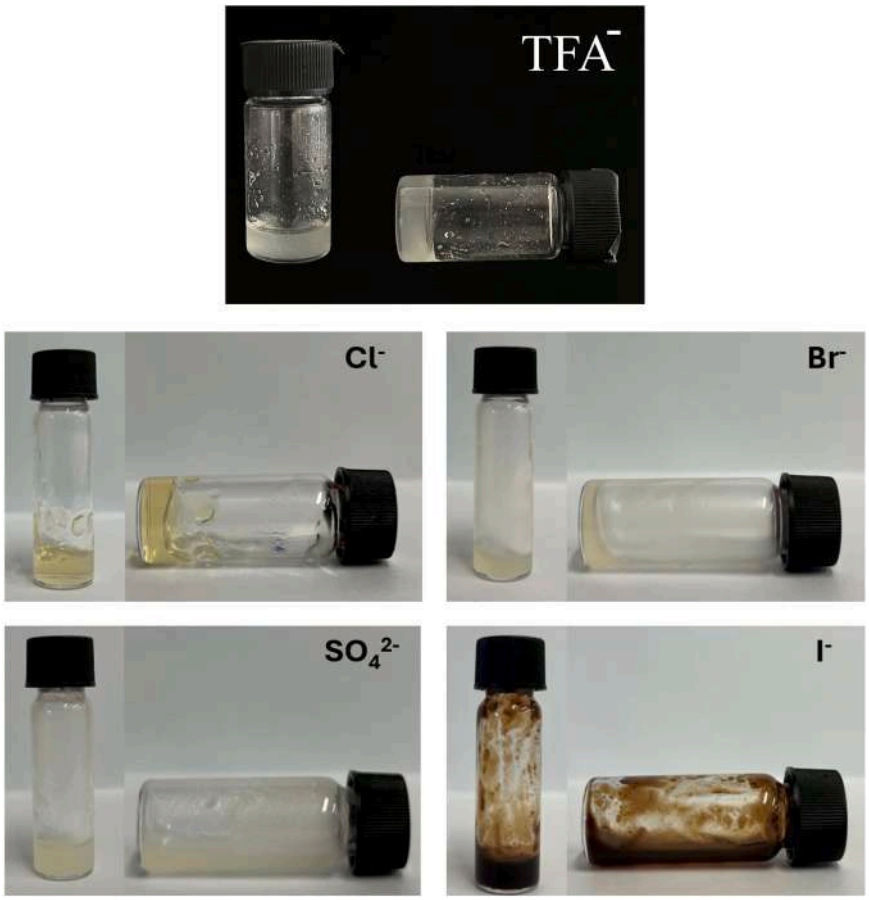


Fig. 1. 3% w/v ACP(65−74)-NH_2 samples in water at 25° C in different the presence of trifluoroacetate, chloride, bromide, sulfate and iodide as counterions.

bearing either Cl^-, Br^-, SO_4^{2-}, I^- or TFA^- as counterions.

Samples containing TFA^-, Cl^- and Br^- form gels, while samples with SO_4^{2-} and I^- produce liquid-like dispersions. For the Br^- sample, a slight rotation of the vial induced a gel-to-sol transition. The I^- sample showed poor dispersibility and appeared as a red suspension (see Fig. 1), requiring vigorous shaking for at least an hour to prepare stable dispersions. The red color was attributed to the amyloid staining properties of iodine [62,63], although we cannot exclude *a priori* a possible (but unlikely) contribution from I_2 and I_3^- formed by partial oxidation of the I^- counterions.

Figures S4 and S5 illustrate pH-responsive behavior of samples (see Supplementary Material). Both gels containing TFA^- and Cl^- undergo a gel-to-sol transition around pH 10, but the sample with TFA^- performs a fully reversible transition, while Cl^- samples show only partial reversibility. Although it undergoes a sol-to-gel transition, the resulting material has a weaker consistency. Samples with Br^- show a non-reversible transition. Neither SO_4^{2-} nor I^- containing dispersions show a transition with pH changes. However, in the presence of I^-, dispersions possess a greater solubility at higher pH.

3.2. Microscopic morphology

3.2.1. Confocal laser scanning microscopy

ThT emission is detectable when the probe is bound to amyloid structures [64]. RBITC preferentially partitions into hydrophobic environments due to its partition coefficient Log $K_{o/w} = 3.22$, estimated with SwissADME [65,66]. However, it also has a moderate water solubility and thus can interact with hydrophilic regions. Fig. 2 shows CLSM images of the samples along with their 3D reconstructions. The I^- sample was excluded from the CLSM experiments because it absorbs strongly at both the excitation and emission wavelengths of ThT and RBITC, attenuating the signal below the detection limit. Blue and red false colors indicate ThT and RBITC emissions, respectively. The images show an overlay of both channels, with magenta indicating where both probes emit.

The counterion effect on microscopic morphology is evident, and each sample showed different morphologies.

The sulfate sample predominantly shows a mix of amyloid and non-amyloid aggregates. These are large and structured, reaching sizes up to 50 μm. A recurring morphology for the largest structures is an amyloid-dominant core with a mixed-morphology contouring the edges.

In the presence of TFA^- we observed a well-defined gel network, characterized by fibrillar structures that incorporate large amyloid aggregates. The fibrillar part displays a combination of red and magenta colors, suggesting the presence of both non-amyloid and amyloid components. In contrast, this well-defined fibrillar network is not observed in the presence of Br^- and Cl^-.

Samples with Cl^- show no higher-order structures, although both ThT and RBITC emissions are evident. This suggests that the structures are too small to be resolved with confocal microscopy.

Samples containing Br^- indicate the presence of an aggregated structure akin to that of SO_4^{2-}, but at a smaller scale. They do not possess a continuous structure, as for the TFA^- sample, but resemble a dense dispersion. These dense aggregate regions have a more interconnected structure than the SO_4^{2-} dispersions.

3.2.2. Atomic force microscopy (AFM)

AFM was used to investigate sample structure at nanometer resolution, complementing the mesoscale information from CLSM images. Topographic images of the samples are shown in Fig. 3. Remarkably, the morphologies detected by AFM are consistent with those observed in CLSM images, showing that the fibrillation and aggregation tendency of the samples is preserved at different length scales.

Although SO_4^{2-} and I^- form dispersions, their overall nanoscale morphology is very different. In the samples containing SO_4^{2-} and I^- fibril-like structures are mostly absent, but only dense aggregates are present. This result is in line with the observation that both SO_4^{2-} and I^- produce dispersions rather than gels.

The TFA^- sample (second panel from the left in Fig. 3) contains well-defined fibrillar structures. These seem to originate from other fibrillar morphologies. In Fig. 3, two smaller helices (green and white arrows) that twist together to form a larger fibril (yellow box) are shown. Such behavior is consistent with the hierarchical nature of amyloid assembly [67,68].

The line profiles were extracted from TFA^- images which show fibril diameters ranging between 20 and 30 nm, including some smaller structures of 6–15 nm (Figures S6 and S7 in the Supplementary Material). The separation distances between fibrils vary. Using the height profile of the fibril in the yellow square shown in Fig. 3, a helix pitch of approximately 40 nm was determined.

In the case of the Cl^- sample, the structure is composed of much smaller fibrils. Also, ThT fluorescence without any corresponding macrostructure in CLSM images suggests that these amyloid fibrils do not form higher-order structures but remain organized at the nanoscale. For Cl^- samples, the line profiles show diameters of the fibrils ranging from 9 to 18 nm, with varying separation distances (see Figure S8 in the

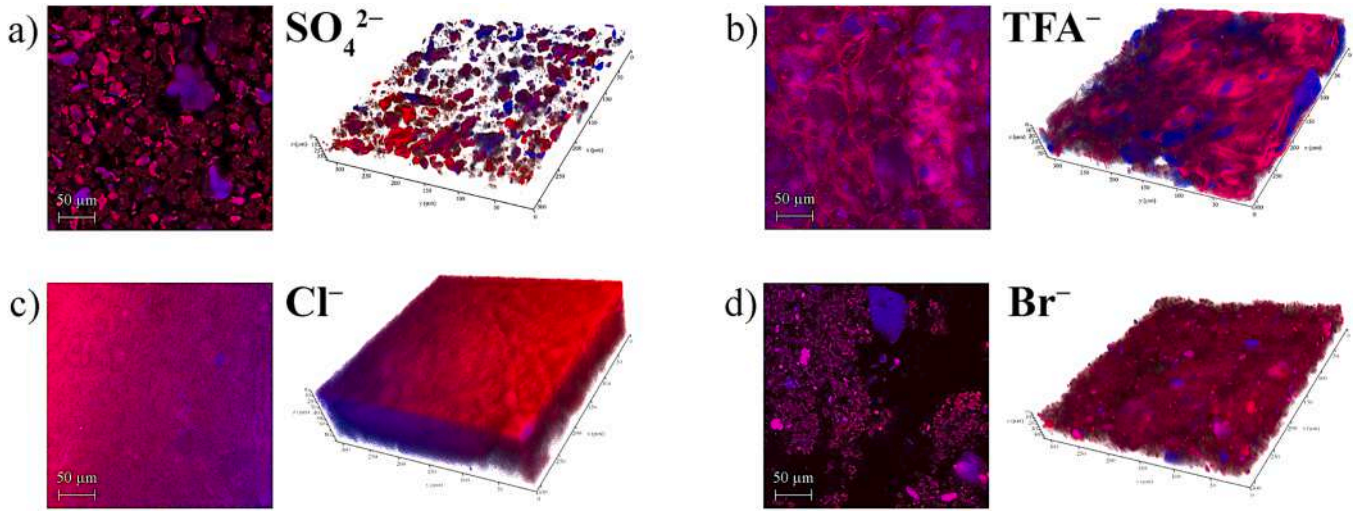


Fig. 2. Confocal Laser Scanning Microscopy images of 3% w/v ACP(65−74)-NH_2 gels or dispersions with counterions a) SO_4^{2-} b) TFA^- c) Cl^- d) Br^- stained with ThT and RBITC. Each panel includes a second image representing a 3D reconstruction of the z-stacked images.

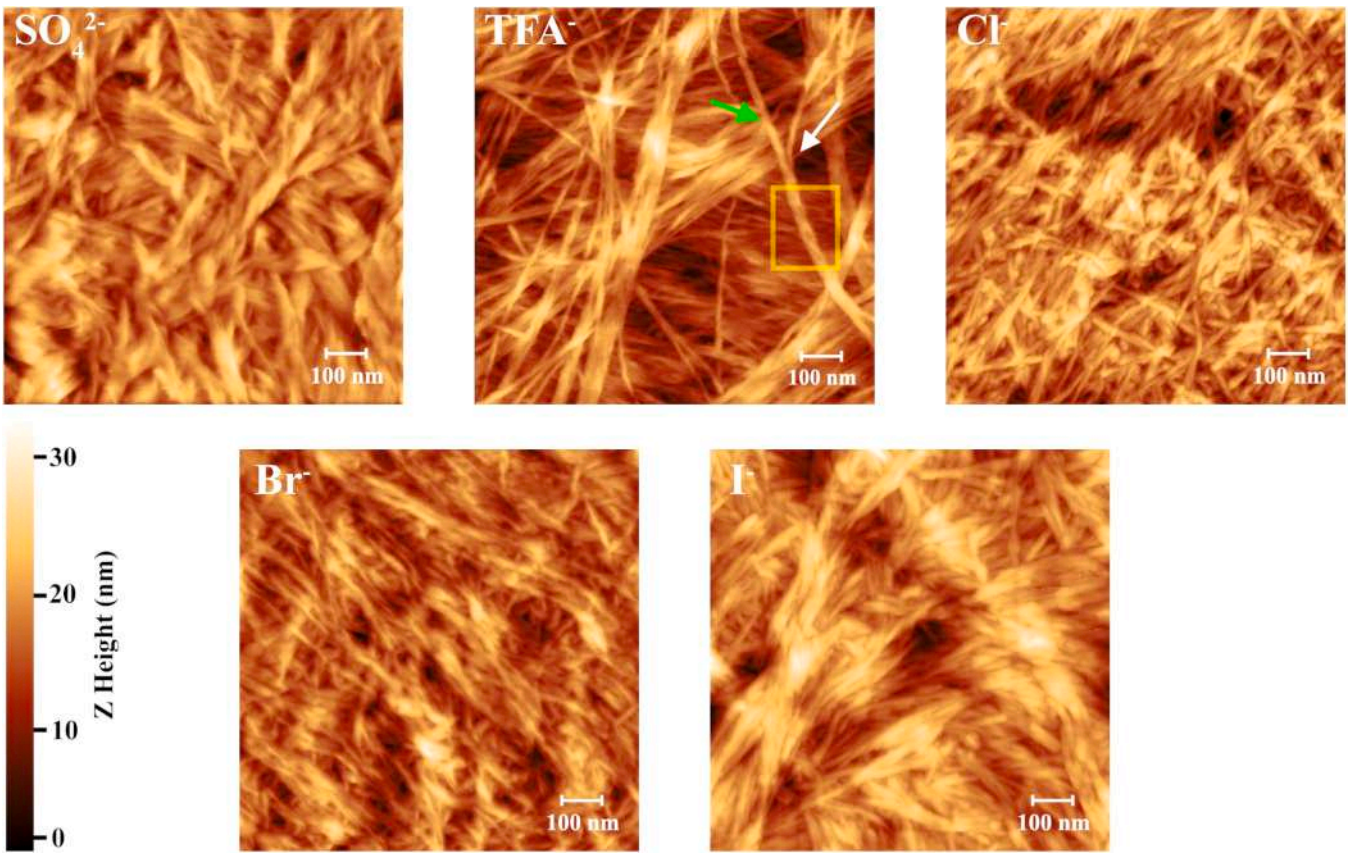


Fig. 3. AFM images of each ACP(65−74)-NH_2 sample containing different counterions. Relative counterions are indicated on each panel.

Supplementary Material). Finally, the Br^- sample displays an intermediate morphology, with fibril-like structures present but no formation of well-defined filaments.

Fig. 4 shows traced and straightened fibrils of the TFA^- sample and their 3D reconstructed models (see the Materials and Methods section). Only data from this sample showed distinct fibrillar structures and were suitable for analysis with Trace_y. The fibrils in the remaining samples were inherently poorly resolved (due to dense or small aggregates), so the software could not be used for further analysis.

Oligomers usually range from 2 to 8 nm in height [69–71] and 5–25 nm in width [69] and typically contain several subunits. According to the literature, oligomers form protofilaments and mature into protofibrils with typical diameters of 2.5–3.1 nm [71,72]. These are usually made of 2 or 3 entangled protofilaments [73]. Protofibrils then mature into fibrils with sizes ranging from 5 to 19 nm in diameter [74,75] and can extend from hundreds of nanometers to several micrometers [75]. The fibrils can then aggregate and form the so-called plaques, with diameters reaching tens of micrometers.

The TFA^- sample shows two right-handed protofibrils (see Fig. 4, panel a, green and white arrows), with heights of 4.9 nm and 3.4 nm, cross-sectional areas of 89.9 nm^2 and 123.6 nm^2 that intertwine to form a larger right-handed fibril with 4 nm height and cross-sectional area of 170 nm^2. The smaller fibrillar structures with helical pitches of 61.6 nm (Fig. 4, panel a, white arrow) and 69.2 nm (Fig. 4, panel a, green arrow) intertwine to form a larger fibril (Fig. 4, panel a, yellow rectangle) with a helical pitch of 32.1 nm. The latter value is close to that obtained by line profile extraction (approximately 40 nm). The helical pitches are much shorter than those reported in the literature for Aβ fibrils (285 nm helical pitch) [74], which is expected given the different peptide sequence and length. Furthermore, the additive discrepancy of the cross-sectional areas ($89.9 + 123.6 \approx 213.6$ nm^2 *vs.* the observed 170.0 nm^2) suggests a tight association and some structural compaction during the intertwining, which corroborates the lower helical pitch found for the larger fibril.

Fig. 4 (panel b) shows two right-handed filaments that differ markedly both in size and structure. The filament indicated inside the green rectangle is thin, with a mean height of 2.4 nm and a cross-sectional area of only 21 nm^2. This fibril is so narrow and thin that it might even represent a single protofilament. It has a helical pitch of 75 nm. In contrast, the filament framed in the cyan rectangle has a mean height of 5.8 nm, more than twice that of the other filament, and is nearly three times wider in cross-section (60 nm^2). This filament has a smaller helical pitch of 64 nm.

3.2.3. *ATR-FTIR spectroscopy*

The secondary structure of proteins and peptides produces distinct signals in the infrared Amide I region in the 1600–1700 cm^{-1} range [76]. These signals can be deconvoluted to separate individual secondary-structure components [76].

When studying amyloid structures, the most significant peaks in the Amide I region are those associated with inter- and intramolecular interactions. Generic β-sheet structures show peaks around 1630 cm^{-1} due to strong intramolecular interactions [54,56–58]. For amyloids and aggregates, the 1630 cm^{-1} peak shifts to lower wavenumbers (below 1620 cm^{-1}) and reflects the strong intermolecular interactions that lend amyloids their characteristic cross-β-sheet structure [54,56–58]. While aggregates in this region are often composed of amyloids, it is important to recall that other non-amyloid components can also form associated nanostructures.

Fig. 5 shows the deconvoluted spectra and their corresponding secondary-structure assignments. Table 1 lists a detailed breakdown of the percentage composition of each structure.

Samples with SO_4^{2-} show a significant peak at 1632 cm^{-1}, suggesting intramolecular β-sheet structures [54,57,58]. According to the

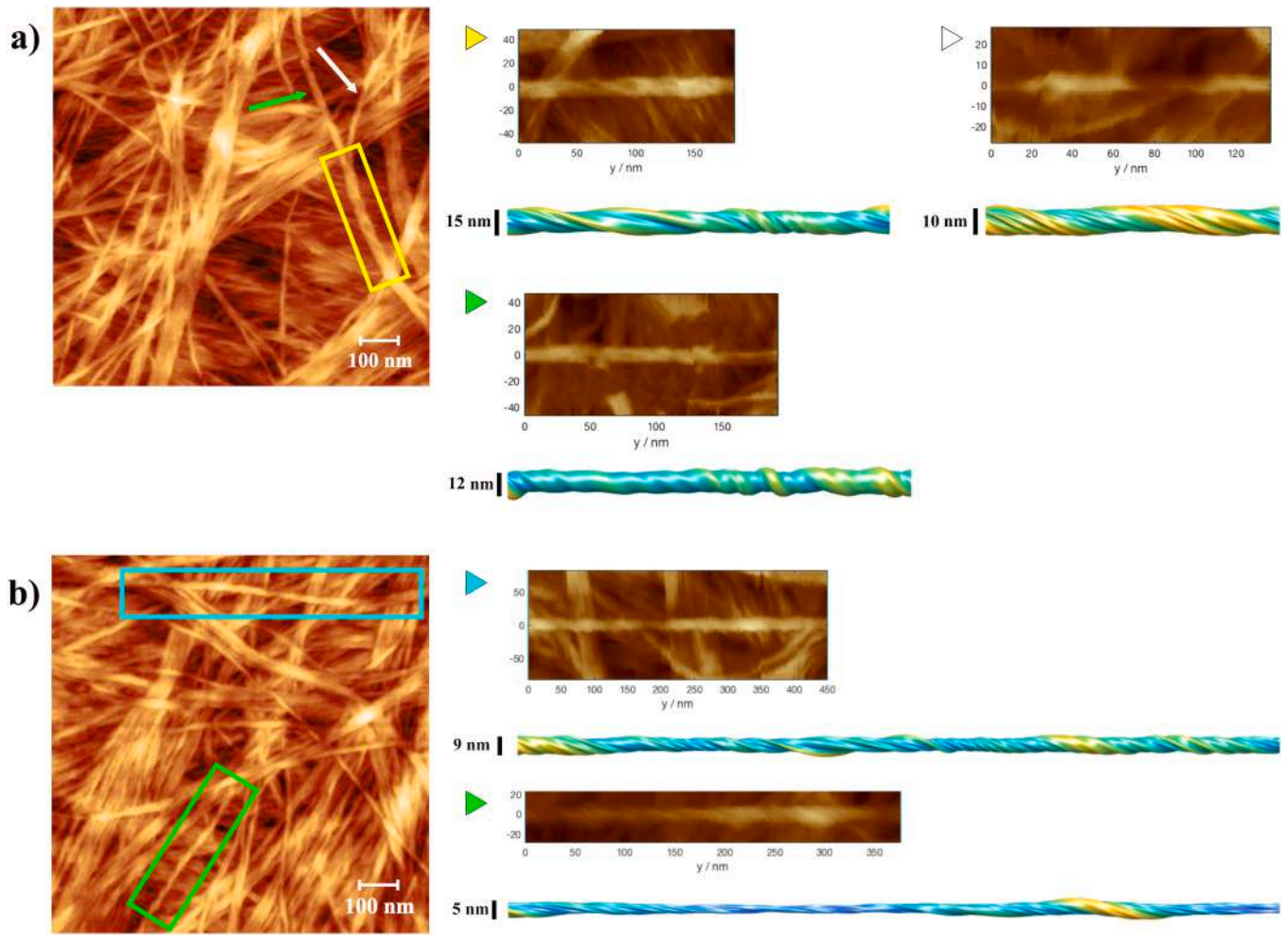


Fig. 4. Two AFM images of the same TFA^- sample (panels a and b), with arrows and rectangles marking the traced fibrils. To the right of each topographic image, the corresponding straightened fibril is shown above and its 3D reconstruction with its cross-sectional diameter below. Color-coded triangles identify each fibril on the AFM image.

literature, the lower wavenumber components reflect the extent of vibrational coupling within the H-bonded β-sheet network, with stronger delocalization giving a larger red shift. On this basis, we interpreted the contributions at 1600 and 1612 cm^{-1} as more extended and ordered β-sheets, larger and more rigid aggregate structures. The component at 1620 cm^{-1} reflects shorter delocalization length and is interpreted as having smaller, more flexible aggregate structures [54,56–58]. Both are consistent with amyloid structures. We note that these descriptors are relative and based on band position alone, so they do not directly measure aggregate dimensions.

Amyloid fibrils can adopt diverse morphologies, so the coexistence of different components is expected [10,11].

A weak peak at 1690 cm^{-1} is observed. This is characteristic of antiparallel β-sheets in the range 1690–1700 cm^{-1}. This signal is diagnostic but does not directly quantify the exact amount of antiparallel β-sheets [56,77,78]. In the literature, the 1695/1630 cm^{-1} intensity ratio has been related to the percentage of antiparallel β-sheets [53,79,80]. The calculated ratios for all samples showed a decreasing antiparallel β-sheet content in the order $SO_4^{2-} > Br^- > I^- > TFA^- > Cl^-$, with a net zero contribution for Cl^- (see Figure S9 in the Supplementary Material).

In the presence of TFA^-, the main contribution is centered at 1630 cm^{-1}. This peak is narrow, indicating a well-correlated system. At higher wavenumbers, we again detected the antiparallel β-sheet signal. Instead, at lower wavenumbers, we observed typical signals of amyloid aggregates. The latter contribution is low, and the main peaks are distributed between 1617 and 1605 cm^{-1}, indicating the presence of quite rigid and large amyloid-based aggregates [54,56–58].

The Cl^- sample lacks the antiparallel β-sheet signal. The 1631 cm^{-1} intramolecular β-sheet structure percentage is notably lower than in samples with other counterions. A prominent peak at 1624 cm^{-1} was assigned to small, flexible amyloid structures, and a much lower-intensity peak at 1612 cm^{-1} was assigned to large and rigid amyloid structures. These are consistent with the CLSM and AFM images and confirm the predominant presence of very small amyloid structures. Furthermore, the different morphology can also be attributed to the presence of only parallel β-sheets.

In the Br−sample, intramolecular β-sheets contribute strongly at 1629 and 1634 cm^{-1}, with the antiparallel β-sheet signal at 1696 cm^{-1}. At lower wavenumbers, 1629, 1617, and 1613 cm^{-1}, significant contributions from both large, highly rigid and small, flexible amyloid-based aggregates are detected. We assigned the 1640–1658 cm^{-1} region to random coil structures, given the dominance of β-sheet/amyloid features of the system [55,57,58,81,82]. However, α-helical signal overlaps in the same range, and deconvolution cannot always disentangle these two contributions [55,57,58,81,82]. Therefore, we cannot exclude that a fraction of α-helical structure contributes to this peak assignment. Notably, the Br^- spectrum shows two resolved peaks at 1647 and 1653 cm^{-1}, making a mixed assignment likely, with the higher wavelength peak consistent with partial α-helical character.

For the I^- samples, a prominent aggregate signal at 1616 cm^{-1} is consistent with rigid and large aggregate structures, alongside a weaker

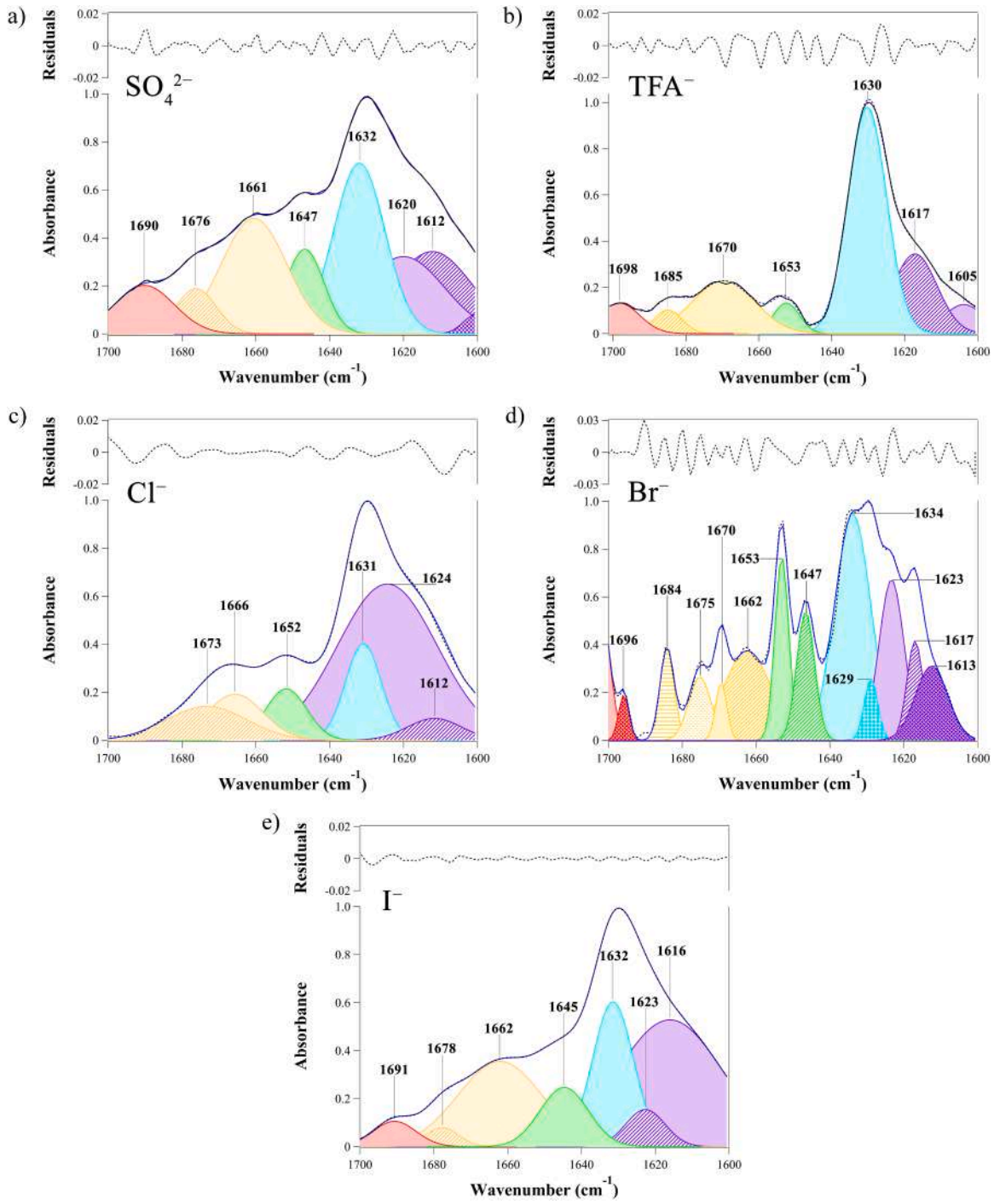


Fig. 5. FTIR spectra of the ACP(65−74)-NH_2 hydrogels or dispersions with counterions: a) SO_4^{2-} b) TFA^- c) Cl^- d) Br^- e) I^-. The Amide I peak deconvolution is colored in purple for amyloid and aggregate structures, in cyan for β-sheets, in green for random coils, in yellow for β-turns and in red for antiparallel β-sheet contribution. The experimental and the fitting spectra are represented by a black dashed and a blue line, respectively.

Table 1
Percentages of secondary structures present in each sample obtained from the deconvolution of the FTIR spectra. The error on the values is ±5%.

	SO_4^{2-}	TFA^-	Cl^-	Br^-	I^-
large aggregates and amyloids	19	6	5	14	42
small aggregates and amyloids	19	20	56	13	5
β-sheets	25	48	12	31	19
random coil with possible α-helical contribution	10	5	8	17	9
β-turns	27	21	19	25	25

component at 1623 cm^{-1}. These structures may be amyloid or non-amyloid aggregates, as the absence of a ThT assay prevents the distinction between the two kinds of particles. We also observed an antiparallel β-sheet structure at 1691 cm^{-1}.

For all samples, the remaining signals are attributed to random coils and β-turns [55,57,58].

3.2.4. Circular dichroism and fluorescence spectroscopy

At very low gelator concentrations, CD and fluorescence spectroscopy allow the investigation of the intrinsic secondary-structure

propensity and, therefore, the earliest counterion-dependent association of the dispersed peptides. Because the conformation and oligomerization propensity of the preassembled peptides influence the fibrillar morphology, these data complement the high concentration results.

CD spectroscopy was performed on ACP(65−74)-NH_2 0.01% w/v dispersions of all samples (Fig. 6, panel a).

The CD spectrum shows no significant changes in secondary-structure percentages (see Table 2 below). The fitting procedure gave normalized root-mean-square deviation (NRMSD) values of approximately 0.04, consistent with an accurate fit. The secondary structure percentages are semi-quantitative, and we did not interpret the small variations between samples as due to significant differences.

All the samples show an alternation between disordered structures and β-organized structures, including antiparallel β-sheets and β-turns. The parallel β-sheet content is negligible in each case.

Ionic species do not significantly affect peptide structure at low concentrations. This is expected, as the counterions are within the peptide fragment, and at 0.01% w/v ACP(65−74)-NH_2, this accounts for 2.1 ppm of counterions. Therefore, specific ion effects are not observed, as expected.

Interestingly, the FTIR analysis of samples at 3% w/v shows a change from antiparallel β-sheet to parallel β-sheet conformation. This is particularly notable in the case of Cl^-, which exclusively forms a parallel β-sheet conformation.

The absorbance of the I^- sample's saturates the spectrophotometer detector across the visible range, including at the excitation and emission wavelengths of ThT and RBITC, and was excluded from the fluorescence spectroscopy experiments. ThT fluorescence is highly specific when bound to well-formed amyloid fibrils. Fig. 6, panel b, shows that all investigated samples exhibit the characteristic amyloid-bound ThT fluorescence signal around 480 nm, indicating a pronounced amyloidogenic propensity of the decapeptide. The signal intensities are similar for samples containing TFA^- and Br^- and higher for SO_4^{2-} and Cl^-; however, these results are qualitative and do not directly reflect the relative amyloid quantity in each sample.

3.3. Rheology – frequency sweeps and thixotropy experiments

The rheological properties of the gel samples were analyzed by means of oscillatory shear experiments to investigate the effect of the different counterions on the macroscopic behavior of the gels. Fig. 7 shows the storage (G') and loss (G'') moduli obtained by frequency sweep experiments for the gels of ACP(65−74)-NH_2 in the presence of TFA^-, Cl^- and Br^-. The samples containing SO_4^{2-} and I^- were not tested since they do not form gels.

Table 2
Secondary structure percentages of ACP(65−74)-NH_2 0.01% w/v aqueous dispersions containing different counterions obtained from CD measurements.

	SO_4^{2-}	TFA^-	Cl^-	Br^-	I^-
antiparallel β-sheets	35	35	37	35	35
parallel β-sheets	1	1	1	1	1
β-turns	18	18	17	16	16
other	46	46	45	48	48

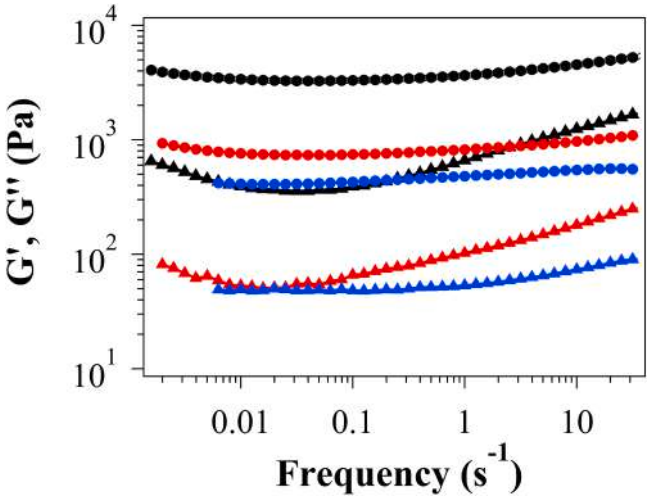


Fig. 7. Frequency sweeps of ACP(65−74)-NH_2 hydrogels in the presence of TFA^- (black), Cl^- (blue) and Br^- (red). The values of G'(circles) and G'' (triangles) are shown for each sample. The experimental error is 3% on each curve.

All the samples exhibit a characteristic solid-like behavior, with a storage modulus nearly independent on the frequency in the investigated range [83]. Moreover, G' is about one order of magnitude larger than G'' and no crossover points are observed, confirming the robust structuredness of the gel network [14].

From the analysis of G' and G'' the effect of the counterion on the gel strength can be ranked as: $TFA^- > Br^- > Cl^-$. These results are consistent with the experimental results from CLSM, AFM and ATR-FTIR measurements, reflecting the changes in the micro and nanostructure induced by the different counterions.

In the presence of TFA^- the well-defined network of fibrillar structures observed in the CLSM and AFM images results in a very high value

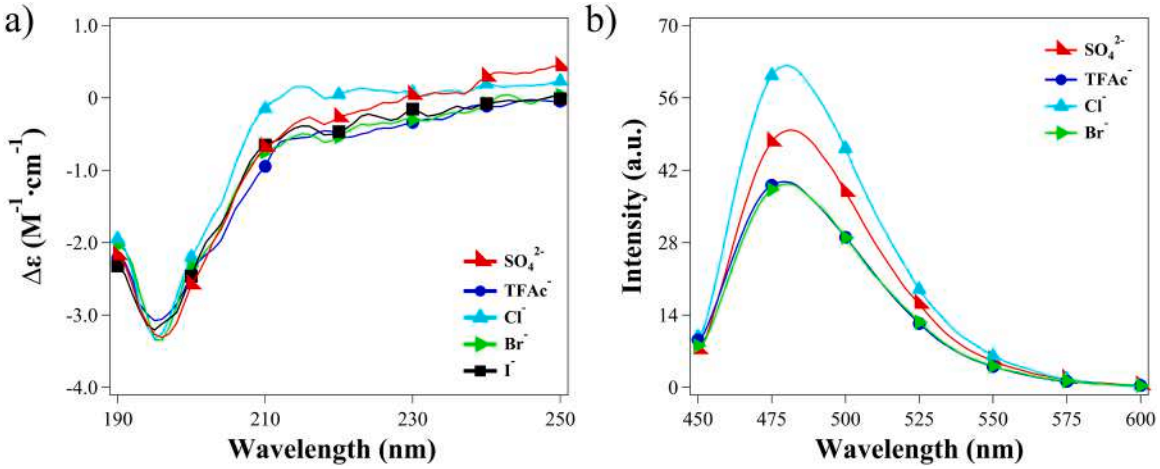


Fig. 6. (a) CD spectrum of ACP(65−74)-NH_2 and (b) ThT fluorescence emission of ACP(65−74)-NH_2 aqueous dispersions at 0.01% w/v concentration in the presence of different counterions.

of *G*'. We recall that the storage modulus is proportional to the network entanglement at constant temperature in gel-like, solid materials [14]. The aggregated structure with interconnected amyloid and non-amyloid clusters found in gel samples containing Br^- results in a slightly higher value of *G*' compared to the Cl^- sample, which reveals the presence of smaller structures with no higher-order aggregation. The gel strength, as reflected by the magnitude of *G*′, follows the order $TFA^- > Br^- > Cl^-$. This trend agrees well with differences in supramolecular morphology and secondary-structure distributions obtained by FTIR. In particular, the TFA^- gel displays both the highest *G*′ and the highest *β*-sheet contribution among the gel-forming samples. Albeit qualitative, this association is a consistent result obtained by Miserez *et al.* [84] in the case of an 8-residue peptide-based hydrogel, in which the gelation process as well as the stiffness of the gel was determined by the transition from 3_{10}-helices to *β*-sheets and their relative abundance among the different secondary structures.

The ability to autonomously repair damage, mimicking biological tissues' natural healing processes, is an extremely valuable property for smart hydrogels and their application in wound healing, drug delivery, and tissue engineering [85]. Another intriguing application of responsive hydrogels is the design of synthetic living systems (or self-replicating systems), in which supramolecular assemblies sustain their own formation through autocatalytic mechanisms [86]. For this reason, the self-healing ability of the ACP(65−74)-NH_2 gels was investigated by means of three interval thixotropy test (3ITT). The results for the samples containing TFA^-, Cl^- and Br^- are shown in Fig. 8.

In the first interval within the linear regime, the storage modulus remains constant for all samples, with negligible fluctuations for TFA^-, confirming a stiff and stable gel network. The increase in the oscillation strain outside the linear region brings about the structural breakdown of the gels, as suggested by the steep decrease in *G*'. When the strain returns to its initial value an immediate and efficient recovery of the storage modulus is attained, demonstrating a remarkable self-healing ability of the gels. While the *G*' recovery is nearly complete in the case of TFA^- and Cl^- (with recovery ratios, RR, of 98 ± 2% and 96 ± 3%, respectively), in the presence of Br^- the RR value drops to 60 ± 4%. These results are consistent with the visual analysis of the samples and the manual shaking trials reported at the beginning of this section. The decrease of *G*" during the high-strain interval and its subsequent recovery after restoring the initial strain parallels the *G*' response, confirming the reversible disruption and reorganization of the viscoelastic network. From the comparison with the results obtained from the ATR-FTIR deconvolution, the reduced self-healing recovery of the sample containing Br^- may be related to the lower overall content of aggregates, amyloids, and *β*-sheets structures (parallel and antiparallel). Moreover, the Br− gel shows a higher percentage of random coils and *α*-helices among the investigated samples (see Table 1). We argue that the combination of these two contributions affects the system's self-assembly behavior, leading to incomplete recovery of the supramolecular structure.

3.4. Specific ion effects

The peptide under investigation bears a single positive charge at the N-terminus where the Asp residue is mostly protonated, while the C-terminus is amidated. In this regime, anion effects are mostly defined by the ion-specific interactions with the peptide and the Coulomb interactions at the N-terminus. Comparing observed morphologies across length scales with known specific anion behavior offers important insights.

We found that both a strongly hydrated kosmotropic ion such as SO_4^{2-} and a poorly hydrated chaotropic ion such as I^- lead to the formation of homogeneous dispersions. However, despite the similar macroscopic behavior, their nanoscale morphologies differ.

The I^- sample shows a high contribution of large, rigid aggregates (42%), with only 5% of smaller aggregates. Weakly hydrated (high polarizability, low charge density) ions can interact directly with C_α-H and CH_2 adjacent to electron-withdrawing groups in the polypeptide backbone [87–90]. Iodide has a strong tendency to bind the backbone and aromatic side chains, and to accumulate at hydrophobic interfaces. Francisco *et al.* showed that iodide's backbone-binding constant to RNase A is about 1.1 M^{-1} versus 0.54 M^{-1} for bromide [90]. Simulations of salts at hydrophobic surfaces show that iodide is enriched near the water/hydrophobic interface, with favorable dispersion interactions at low-dielectric surfaces [91]. Gas-phase infrared multiphoton dissociation (IRMPD) experiments combined with density functional theory (DFT) calculations on isolated tyrosine show that the most stable phenol-bound I^- complex is about 6.8 $kJ{\cdot}mol^{-1}$ more stable than the reference geometry, and more favorable than for Br^- or Cl^- [92].

By analogy, in our system I^- is expected to adsorb to the backbone, accumulate near isoleucine and valine residues, and interact with the tyrosine phenol ring. Our experimental results suggest that iodide preferentially stabilizes more extended and ordered *β*-sheets, leading to larger, more rigid aggregate structures. The exact nature of these aggregates is unknown, and they may be either amyloid or non-amyloid. In the latter case, the interactions described above can in fact perturb the conformational equilibrium and disrupt the H-bonding needed to seed cross-*β* formations, favoring disordered aggregation. However, the possible presence of I_3^- and/or other polyiodide species complicates the interpretation, and the observed effects may reflect a convolution of

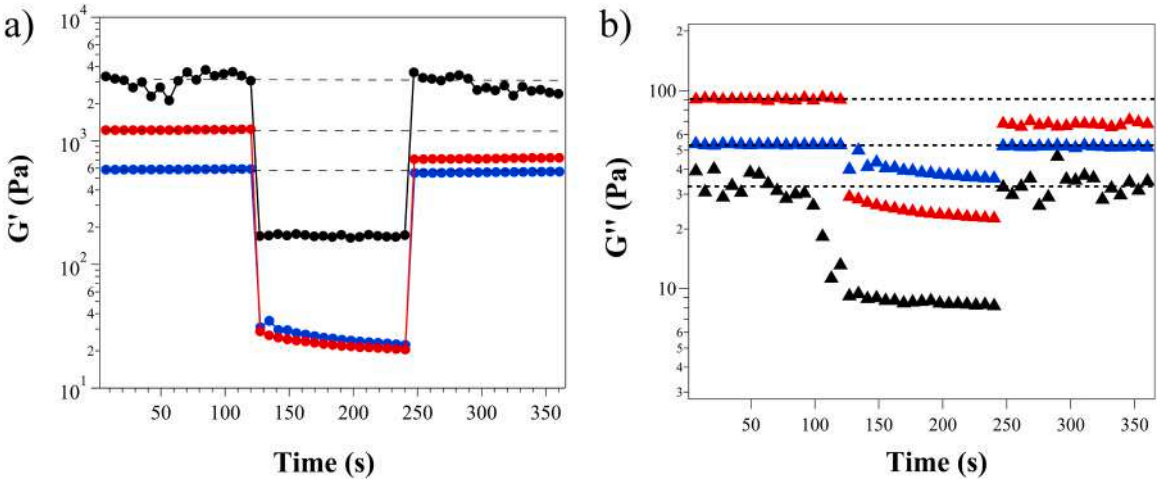


Fig. 8. Three interval thixotropy test (3ITT) results for ACP(65−74)-NH_2 gels in the presence of TFA^- (black), Cl^- (blue) and Br^- (red): (a) storage modulus *G*' and (b) loss modulus *G*". The dotted lines serve as guides for the eye.

contributions from several iodine-based species.

In the presence of sulfate ions, the intermolecular β-sheet content is evenly partitioned between large, rigid aggregates and smaller, flexible aggregates. It shows very organized structures with mixed morphology, mostly stained by ThT.

Sulfate is a strongly hydrated kosmotrope that competes for water and therefore can strip the peptide's hydration shell, promoting salting-out and aggregation [35,89]. In our system, SO_4^{2-} should be repelled from the peptide backbone and hydrophobic core but should strongly interact with the N-terminus. It does not perturb intra- and intermolecular interactions between peptide chains, allowing the system to progress toward cross-β structure and amyloid formation. This fits our observations of large, micron-scale aggregates containing amyloid structure.

Instead, gels form in the presence of mild kosmotropic and chaotropic ions. Notably, the strongest gel forms with the kosmotropic TFA^-, which shows the lowest intermolecular β-sheet content at 26% and the highest intramolecular β-sheet content at 48%. Its morphology shows large amyloid aggregates wrapped in long wormlike structures.

The isotropic average polarizability of TFA^- is 6.393 $Å^3$ [93]. Higher polarizabilities lead to stronger van der Waals interactions, which are important in aromatic-ring interactions [35]. Solid-state NMR studies of a phenylalanine-rich peptide undergoing liquid-liquid phase separation provide an important insight. Lim *et al.* showed that TFA^- ions partition into the condensed peptide phase to form a structured complex, in which a single TFA^- ion intercalates between two stacked aromatic rings [93]. They also showed that TFA^- remains in spatial proximity to backbone amide protons [93].

Furthermore, in polyatomic ions, anisotropic polarizability and molecular geometry can critically affect ion interactions and create multiple interaction modes that are not accessible to spherical or monoatomic ions [35,43,94].

While both TFA^- and I^- can approach the backbone and tyrosine side chains, the kosmotropic nature and anisotropic polarizability of TFA^- appear to stabilize ordered fibrillar assemblies through multiple dispersion contacts with aromatic and backbone regions.

Cl^- produces weaker gels with an all-parallel β-sheet conformation and the lowest amount of β-turn components. It exhibits the lowest intramolecular β-sheet contribution at 12% and the highest intermolecular β-sheet content at 61%, with the dominance of smaller, less rigid aggregates with only a few in large, rigid aggregates. The aggregate structures are much smaller, below the CSLM resolution. However, Cl^- has the highest propensity to form amyloid fibrils, even at low concentrations.

Chloride is a borderline mild ion in the Hofmeister series, lying in the midpoint between kosmotropes and chaotropes. It shows negligible specific binding to backbone C_α-H and adjacent CH_2 groups compared to more chaotropic anions in both short-peptide and protein models [89,90]. Cl^- mainly neutralizes the N-terminal charge and slightly alters the hydration features of our system. This is consistent with peptide amphiphile studies where Cl^- lies in the regime that promotes orderly β-sheet nanofiber formation by screening cationic headgroups while leaving the hydrophobic tails free to pack [95] and matches our observation of many small amyloid fibrils with no large micron-scale aggregates.

For bromide, we expect an intermediate behavior between chloride and iodide. Br^- is a chaotrope and disrupts the hydrogen bonding network, but to a lesser extent than I^-. It contributes similarly to intramolecular and intermolecular β-sheets, at 31% and 27%, respectively. Br^- forms small, organized regions made up entirely of large amyloid aggregates, with some smaller structures stained by RBITC and ThT.

As mentioned before, Br^- binds to the peptide backbone more weakly than iodide, and an IRMPD study on isolated tyrosine confirms that phenol-bound Br^- complexes are stable, though to a lesser degree than I^- [92]. Br^- should still interact with the N-terminus but also starts to bind to the backbone, to hydrophobic and tyrosine residues. This overall behavior is in line with a mixed pathway, as some follow a cross-β nucleation route, while others are captured into less ordered aggregates.

4. Conclusions

Our results show that counterions play an active role in the self-assembly. The ion identity is not only a toxicological concern but a distinctive variable in the system. While TFA^- substitution is routinely performed to avoid toxic effects, particularly in therapeutic applications, this is not the complete picture. The presence of different ions can modify the self-assembly pathways and give rise to entirely different supramolecular adducts for the same peptide under otherwise identical conditions.

Ions can affect a system in different, and sometimes opposing, ways. Hydration, polarizability, interfacial features, and molecular geometry all contribute unique interactions. The observed global outcome results from simultaneously occurring mechanisms. Sometimes a single dominant mechanism is present and can define a general trend. The overall effect can simply result from multiple interactions operating together.

The specific nature of a counterion and therefore its interactions with both solvent and solutes determines the final self-assembled state of the peptide and the resulting amyloid morphology. This study shows that ion-peptide interactions are crucial for amyloid nucleation and depend on the ion's specific nature.

Similar macroscopic behavior can emerge from completely different nanoscale and microscale organizations. I^- is a large, weakly hydrated, and highly polarizable chaotropic anion capable of significant dispersion interactions. SO_4^{2-} is a strongly kosmotropic, highly hydrated ion that promotes amyloid formation. The preferential hydration mechanism associated with kosmotropes reduces protein-solvent interactions, lowers the free energy barrier for peptide chain contact, and drives aggregation.

Molecular geometry is often overlooked for polyatomic ions. Ions are not point charges, they have a particular shape and an anisotropic charge distribution across the structure that in turn results in a significant anisotropy in the polarizability. In these cases, an ion can present multiple interaction sites and coordinate solutes and solvent in ways inaccessible to spherical, isotropic, monoatomic ions. This is mostly evident in the case of TFA^-, whose asymmetric fluorinated structure and strong electrostatic and H-bond accepting character produce secondary structure, nanoscale, and microscale morphologies distinctly different from those seen with the other anions. Although SO_4^{2-} is also a polyatomic ion, its tetrahedral geometry gives a different influence on amyloid assembly compared to the asymmetric TFA^-.

Chloride needs a separate argument. Positioned at the boundary between strong kosmotropic and chaotropic anions, it behaves as a mild ion that screens charge while preserving the intermolecular packing geometry required for fibril growth. Among the ions examined, it yields the highest amyloid propensity and forms fibrillar aggregates with all parallel β-sheet secondary structure, without producing the large micron-scale assemblies observed with the other ions. The Cl^- sample can be regarded as a simplified synthetic reference incorporating a physiologically relevant counterion given its high abundance in physiological extracellular fluids, though it does not reproduce the full ionic complexity of natural extracellular environments.

Overall, our data demonstrate that the choice of counterion must be regarded as a true experimental variable. Complete counterion exchange is therefore essential for obtaining meaningful and physiologically relevant conclusions from synthetic peptide systems. In particular, replacing residual trifluoroacetate with chloride is not only desirable from a toxicological standpoint but also necessary to avoid counterion-driven artifacts in studies of amyloid formation, supramolecular morphology, and peptide material properties.

CRediT authorship contribution statement

Mert Acar: Writing – review & editing, Writing – original draft, Visualization, Validation, Methodology, Investigation, Formal analysis, Data curation, Conceptualization. **Duccio Tatini:** Writing – review & editing, Writing – original draft, Visualization, Methodology, Investigation, Formal analysis. **Ilaria Clemente:** Writing – original draft, Visualization, Validation, Investigation, Formal analysis. **Luigi Talarico:** Writing – original draft, Visualization, Validation, Investigation, Formal analysis. **Agnese Magnani:** Writing – review & editing, Resources, Methodology. **Michael Quagliata:** Writing – original draft, Methodology, Investigation. **Francesca Nuti:** Data curation, Methodology, Validation, Writing – review & editing. **Anna Maria Papini:** Writing – original draft, Resources, Methodology. **Pierandrea Lo Nostro:** Writing – review & editing, Writing – original draft, Supervision, Resources, Methodology, Funding acquisition, Conceptualization.

Funding

None.

Associated content

Supplementary Material**.** The following files are available free of charge.

Table showing buffer composition, Figures of calibration curves for TFA; FTIR spectrum of TFA control; amplitude sweeps; pH responsive behavior; AFM height profile images of TFA^- and Cl^- samples; box plot of 1695/1630 cm^{-1} ratios (PDF).

Declaration of Competing Interest

The authors declare that they have no known competing financial interests or personal relationships that could have appeared to influence the work reported in this paper.

Acknowledgment

The authors acknowledge Lorenzo Pacini for his assistance in the solid phase peptide synthesis, and Alberto Fidi for carrying out some of the experimental work.

Appendix A. Supporting information

Supplementary data associated with this article can be found in the online version at doi:10.1016/j.colsurfa.2026.142043.

Data availability

Data will be made available on request.

References

[1] T.S. Chisholm, C.A. Hunter, A closer look at amyloid ligands, and what they tell us about protein aggregates, Chem. Soc. Rev. 53 (2024) 1354–1374, https://doi.org/10.1039/D3CS00518F.
[2] D.J. Rinauro, F. Chiti, M. Vendruscolo, R. Limbocker, Misfolded protein oligomers: mechanisms of formation, cytotoxic effects, and pharmacological approaches against protein misfolding diseases, Mol. Neurodegener. 19 (2024) 20, https://doi.org/10.1186/s13024-023-00651-2.
[3] J. Wu, J. Wu, T. Chen, J. Cai, R. Ren, Protein aggregation and its affecting mechanisms in neurodegenerative diseases, Neurochem. Int. 180 (2024) 105880, https://doi.org/10.1016/j.neuint.2024.105880.
[4] L. Agnello, C.M. Gambino, A.M. Ciaccio, F. Cacciabaudo, D. Massa, A. Masucci, M. Tamburello, R. Vassallo, M. Midiri, C. Scazzone, M. Ciaccio, From Amyloid to Synaptic Dysfunction: Biomarker-Driven Insights into Alzheimer's Disease, Curr. Issues Mol. Biol. 47 (2025) 580, https://doi.org/10.3390/cimb47080580.
[5] A. Mahboob, H. Ali, A. AlNaimi, M. Yousef, M. Rob, N.A. Al-Muhannadi, D.K. L. Senevirathne, A. Chaari, Immunotherapy for Parkinson's Disease and Alzheimer's Disease: A Promising Disease-Modifying Therapy, Cells 13 (2024) 1527, https://doi.org/10.3390/cells13181527.
[6] G. Zuccon, A. Darnal, E. Longo, S. D'Aronco, E. Boselli, P. Orlando, A. Ceccon, Molecular mechanisms of amyloid inhibition: an NMR-driven framework with polyphenols as a case study, Front. Mol. Biosci. 12 (2025) 1676927, https://doi.org/10.3389/fmolb.2025.1676927.
[7] E. Pechkova, S. Fiordoro, A. Izzotti, C. Riekel, Recent Advances in Amyloids Structural Studies and Thin Film Applications, Molecules 30 (2025) 2908, https://doi.org/10.3390/molecules30142908.
[8] F. Chiti, C.M. Dobson, Protein Misfolding, Functional Amyloid, and Human Disease, Annu. Rev. Biochem. 75 (2006) 333–366, https://doi.org/10.1146/annurev.biochem.75.101304.123901.
[9] T.P.J. Knowles, M. Vendruscolo, C.M. Dobson, The amyloid state and its association with protein misfolding diseases, Nat. Rev. Mol. Cell. Biol. 15 (2014) 384–396, https://doi.org/10.1038/nrm3810.
[10] M.G. Iadanza, M.P. Jackson, E.W. Hewitt, N.A. Ranson, S.E. Radford, A new era for understanding amyloid structures and disease, Nat. Rev. Mol. Cell. Biol. 19 (2018) 755–773, https://doi.org/10.1038/s41580-018-0060-8.
[11] K.L. Stewart, E. Hughes, E.A. Yates, D.A. Middleton, S.E. Radford, Molecular Origins of the Compatibility between Glycosaminoglycans and Aβ40 Amyloid Fibrils, J. Mol. Biol. 429 (2017) 2449–2462, https://doi.org/10.1016/j.jmb.2017.07.003.
[12] N. Singh, K. Patel, A. Navalkar, P. Kadu, D. Datta, D. Chatterjee, S. Mukherjee, R. Shaw, N. Gahlot, A. Shaw, S. Jadhav, S.K. Maji, Amyloid fibril-based thixotropic hydrogels for modeling of tumor spheroids in vitro, Biomaterials 295 (2023) 122032, https://doi.org/10.1016/j.biomaterials.2023.122032.
[13] W. Wang, B. He, T. Xiao, M. Xu, B. Liu, Y. Gao, Y. Chen, J. Li, B. Ge, J. Ma, H. Ge, Bioinspired Amyloid Fibril-Based Hydrogel with Engineering Programable Functionalities for Diverse Applications, Adv. Funct. Mater. 33 (2023) 2209441, https://doi.org/10.1002/adfm.202209441.
[14] M. Acar, D. Tatini, A. Fidi, L. Pacini, M. Quagliata, F. Nuti, A.M. Papini, P. Lo Nostro, A Promising Compound for Green Multiresponsive Materials Based on Acyl Carrier Protein, Langmuir 40 (2024) 12381–12393, https://doi.org/10.1021/acs.langmuir.4c00476.
[15] S. Chowdhury, N. Sarkar, Exploring the potential of amyloids in biomedical applications: A review, Biotechnol. Bioeng. 121 (2024) 26–38, https://doi.org/10.1002/bit.28569.
[16] R.S. Jacob, D. Ghosh, P.K. Singh, S.K. Basu, N.N. Jha, S. Das, P.K. Sukul, S. Patil, S. Sathaye, A. Kumar, A. Chowdhury, S. Malik, S. Sen, S.K. Maji, Self healing hydrogels composed of amyloid nano fibrils for cell culture and stem cell differentiation, Biomaterials 54 (2015) 97–105, https://doi.org/10.1016/j.biomaterials.2015.03.002.
[17] U. Shimanovich, I. Efimov, T.O. Mason, P. Flagmeier, A.K. Buell, A. Gedanken, S. Linse, K.S. Åkerfeldt, C.M. Dobson, D.A. Weitz, T.P.J. Knowles, Protein Microgels from Amyloid Fibril Networks, ACS Nano 9 (2015) 43–51, https://doi.org/10.1021/nn504869d.
[18] M. Díaz-Caballero, S. Navarro, S. Ventura, Functionalized Prion-Inspired Amyloids for Biosensor Applications, Biomacromolecules 22 (2021) 2822–2833, https://doi.org/10.1021/acs.biomac.1c00222.
[19] A.J. Baldwin, R. Bader, J. Christodoulou, C.E. MacPhee, C.M. Dobson, P.D. Barker, Cytochrome Display on Amyloid Fibrils, J. Am. Chem. Soc. 128 (2006) 2162–2163, https://doi.org/10.1021/ja0565673.
[20] S. Peña-Díaz, W.P. Olsen, H. Wang, D.E. Otzen, Functional Amyloids: The Biomaterials of Tomorrow? Adv. Mater. 36 (2024) 2312823 https://doi.org/10.1002/adma.202312823.
[21] S.S. Yadav, P.K. Padhy, A.K. Singh, S. Sharma, Tanu, S. Fatima, A. Sinha, R. Tariq, S.K. Varsha, S. Sharma, Priya, Advancements in amyloid-based biological materials for healthcare, environmental and sensing applications, Mater. Adv. 5 (2024) 4078–4090, https://doi.org/10.1039/D3MA00969F.
[22] V. Kumar, N. Sinha, A.K. Thakur, Necessity of regulatory guidelines for the development of amyloid based biomaterials, Biomater. Sci. 9 (2021) 4410–4422, https://doi.org/10.1039/D1BM00059D.
[23] C. Li, A. Iscen, H. Sai, K. Sato, N.A. Sather, S.M. Chin, Z. Álvarez, L.C. Palmer, G. C. Schatz, S.I. Stupp, Supramolecular–covalent hybrid polymers for light-activated mechanical actuation, Nat. Mater. 19 (2020) 900–909, https://doi.org/10.1038/s41563-020-0707-7.
[24] H. Wang, Z. Yang, Short-peptide-based molecular hydrogels: novel gelation strategies and applications for tissue engineering and drug delivery, Nanoscale 4 (2012) 5259, https://doi.org/10.1039/c2nr31149f.
[25] S. Li, Q. Yu, H. Li, M. Chen, Y. Jin, D. Liu, Self-Assembled Peptide Hydrogels in Regenerative Medicine, Gels 9 (2023) 653, https://doi.org/10.3390/gels9080653.
[26] V. Gomes, S.R.S. Veloso, M.A. Correa-Duarte, P.M.T. Ferreira, E.M.S. Castanheira, Tuning Peptide-Based Hydrogels: Co-Assembly with Composites Driving the Highway to Technological Applications, Int. J. Mol. Sci. 24 (2022) 186, https://doi.org/10.3390/ijms24010186.
[27] Y. Lin, J. Lin, S. Peng, C. Yeh, W. Chen, T. Chang, M. Liu, C. Lai, Multifunctional gentamicin supplementation of poly(γ-glutamic acid)-based hydrogels for wound dressing application, J. Appl. Polym. Sci. 120 (2011) 1057–1068, https://doi.org/10.1002/app.33249.
[28] S.-Y. Qin, Y. Pei, X.-J. Liu, R.-X. Zhuo, X.-Z. Zhang, Hierarchical self-assembly of a β-amyloid peptide derivative, J. Mater. Chem. B 1 (2013) 668–675, https://doi.org/10.1039/C2TB00105E.
[29] Y. Lai, F. Li, Z. Zou, M. Saeed, Z. Xu, H. Yu, Bio-inspired amyloid polypeptides: From self-assembly to nanostructure design and biotechnological applications, Appl. Mater. Today 22 (2021) 100966, https://doi.org/10.1016/j.apmt.2021.100966.

[30] A. Udomprasert, M.N. Bongiovanni, R. Sha, W.B. Sherman, T. Wang, P.S. Arora, J. W. Canary, S.L. Gras, N.C. Seeman, Amyloid fibrils nucleated and organized by DNA origami constructions, Nat. Nanotechnol. 9 (2014) 537–541, https://doi.org/10.1038/nnano.2014.102.
[31] K. Sikora, D. Neubauer, M. Jaśkiewicz, W. Kamysz, Citropin 1.1 Trifluoroacetate to Chloride Counter-Ion Exchange in HCl-Saturated Organic Solutions: An Alternative Approach, Int. J. Pept. Res. Ther. 24 (2018) 265–270, https://doi.org/10.1007/s10989-017-9611-7.
[32] Y. Liu, Y. Huang, L. Yang, Y. Gao, Z. Jia, T. Liu, B. Su, C. Wang, L. Jin, D. Zhang, The Effects of Counter-Ions on Peptide Structure, Activity, and Applications, Biomolecules 15 (2025) 1567, https://doi.org/10.3390/biom15111567.
[33] S. Roux, E. Zékri, B. Rousseau, M. Paternostre, J. Cintrat, N. Fay, Elimination and exchange of trifluoroacetate counter-ion from cationic peptides: a critical evaluation of different approaches, J. Pept. Sci. 14 (2008) 354–359, https://doi.org/10.1002/psc.951.
[34] V. Erckes, A. Streuli, L. Chamera Rendueles, S.D. Krämer, C. Steuer, Towards a Consensus for the Analysis and Exchange of TFA as a Counterion in Synthetic Peptides and Its Influence on Membrane Permeation, Pharmaceuticals 18 (2025) 1163, https://doi.org/10.3390/ph18081163.
[35] P. Lo Nostro, B.W. Ninham, Hofmeister Phenomena: An Update on Ion Specificity in Biology, Chem. Rev. 112 (2012) 2286–2322, https://doi.org/10.1021/cr200271j.
[36] K.P. Gregory, G.R. Elliott, H. Robertson, A. Kumar, E.J. Wanless, G.B. Webber, V.S. J. Craig, G.G. Andersson, A.J. Page, Understanding specific ion effects and the Hofmeister series, Phys. Chem. Chem. Phys. 24 (2022) 12682–12718, https://doi.org/10.1039/D2CP00847E.
[37] Y. Zhang, P.S. Cremer, The inverse and direct Hofmeister series for lysozyme, Proc. Natl. Acad. Sci. 106 (2009) 15249–15253, https://doi.org/10.1073/pnas.0907616106.
[38] B. Lv, Q. Guo, X. Ji, L. Gai, L. Liu, Hofmeister Effect Mediated Conductivity of Hydrogel Electrolytes for High Performance Supercapacitor, Batter. Supercaps 7 (2024) e202400245, https://doi.org/10.1002/batt.202400245.
[39] B. Kang, H. Tang, Z. Zhao, S. Song, Hofmeister Series: Insights of Ion Specificity from Amphiphilic Assembly and Interface Property, ACS Omega 5 (2020) 6229–6239, https://doi.org/10.1021/acsomega.0c00237.
[40] C.L. Henry, V.S.J. Craig, The Link between Ion Specific Bubble Coalescence and Hofmeister Effects Is the Partitioning of Ions within the Interface, Langmuir 26 (2010) 6478–6483, https://doi.org/10.1021/la9039495.
[41] D. Tatini, D. Ciardi, C. Sofroniou, B.W. Ninham, P. Lo Nostro, Physicochemical characterization of green sodium oleate-based formulations. Part 2. Effect of anions, J. Colloid Interface Sci. 617 (2022) 399–408, https://doi.org/10.1016/j.jcis.2022.01.135.
[42] D. Tatini, E. Anselmi, G. Cabrucci, M. Acar, B.W. Ninham, P. Lo Nostro, Ionochromism, solvatochromism and effect of dissolved gases on the spectral properties of bromothymol blue, J. Mol. Liq. 365 (2022) 120196, https://doi.org/10.1016/j.molliq.2022.120196.
[43] M. Acar, D. Tatini, B.W. Ninham, F. Rossi, N. Marchettini, P. Lo Nostro, The Lyotropic Nature of Halates: An Experimental Study, Molecules 27 (2022) 8519, https://doi.org/10.3390/molecules27238519.
[44] M. Acar, D. Tatini, M.A. Budroni, B.W. Ninham, M. Rustici, F. Rossi, P. Lo Nostro, Specific anion effects on urease activity: A Hofmeister study, Colloids Surf. B Biointerfaces 236 (2024) 113789, https://doi.org/10.1016/j.colsurfb.2024.113789.
[45] P. Lo Nostro, N. Peruzzi, M. Severi, B.W. Ninham, P. Baglioni, Asymmetric Partitioning of Anions in Lysozyme Dispersions, J. Am. Chem. Soc. 132 (2010) 6571–6577, https://doi.org/10.1021/ja101603n.
[46] M. Lagi, P. Lo Nostro, E. Fratini, B.W. Ninham, P. Baglioni, Insights into Hofmeister Mechanisms: Anion and Degassing Effects on the Cloud Point of Dioctanoylphosphatidylcholine/Water Systems, J. Phys. Chem. B 111 (2007) 589–597, https://doi.org/10.1021/jp065769y.
[47] H. Willmer, S. Adams, J. De-Alwis, P. Hancock, Routine determination of trifluoroacetic acid (TFA) and difluoroacetic acid (DFA) in surface and drinking water by direct injection using UPLC-MS/MS, Application Note 720007765, Waters Corporation, Milford, MA, USA, 2022. https://www.waters.com/nextgen/us/en/library/application-notes/2022/Routine-Determination-of-Trifluoroacetic-Acid-TFA-and-Difluoroacetic-Acid-DFA-in-Surface-and-Drinking-Water-by-Direct-Injection-Using-UPLC-MS-MS.html (accessed 13 September 2026).
[48] P. Klapetek. Quantitative data processing in scanning probe microscopy: SPM applications for nanometrology, 2nd ed, Elsevier, Amsterdam, 2018.
[49] D. Nečas, P. Klapetek, Gwyddion: an open-source software for SPM data analysis, Open. Phys. 10 (2012) 181–188, https://doi.org/10.2478/s11534-011-0096-2.
[50] W.-F. Xue, Trace_y: Software algorithms for structural analysis of individual helical filaments by three-dimensional contact point reconstruction atomic force microscopy, Structure 33 (2025) 363–371.e2, https://doi.org/10.1016/j.str.2024.11.007.
[51] L. Lutter, C.J. Serpell, M.F. Tuite, L.C. Serpell, W.-F. Xue, Three-dimensional reconstruction of individual helical nano-filament structures from atomic force microscopy topographs, Biomol. Concepts 11 (2020) 102–115, https://doi.org/10.1515/bmc-2020-0009.
[52] L.D. Aubrey, L. Lutter, K. Fennell, T.J. Purton, N.L. Ward, L.C. Serpell, W.-F. Xue, Structural reconstruction of individual filaments in Aβ42 fibril populations assembled in vitro reveal rare species that resemble ex vivo amyloid polymorphs from human brains, Commun. Chem. 8 (2025) 358, https://doi.org/10.1038/s42004-025-01741-6.
[53] E. Cerf, R. Sarroukh, S. Tamamizu-Kato, L. Breydo, S. Derclaye, Y.F. Dufrêne, V. Narayanaswami, E. Goormaghtigh, J.-M. Ruysschaert, V. Raussens, Antiparallel β-sheet: a signature structure of the oligomeric amyloid β-peptide, Biochem. J. 421 (2009) 415–423, https://doi.org/10.1042/BJ20090379.
[54] S. Vonhoff, J. Condliffe, H. Schiffter, Implementation of an FTIR calibration curve for fast and objective determination of changes in protein secondary structure during formulation development, J. Pharm. Biomed. Anal. 51 (2010) 39–45, https://doi.org/10.1016/j.jpba.2009.07.031.
[55] B. Shivu, S. Seshadri, J. Li, K.A. Oberg, V.N. Uversky, A.L. Fink, Distinct β-Sheet Structure in Protein Aggregates Determined by ATR–FTIR Spectroscopy, Biochemistry 52 (2013) 5176–5183, https://doi.org/10.1021/bi400625v.
[56] S.D. Moran, M.T. Zanni, How to Get Insight into Amyloid Structure and Formation from Infrared Spectroscopy, J. Phys. Chem. Lett. 5 (2014) 1984–1993, https://doi.org/10.1021/jz500794d.
[57] J. Kong, S. Yu, Fourier Transform Infrared Spectroscopic Analysis of Protein Secondary Structures, Acta Biochim. Biophys. Sin. 39 (2007) 549–559, https://doi.org/10.1111/j.1745-7270.2007.00320.x.
[58] X. Hu, D. Kaplan, P. Cebe, Determining Beta-Sheet Crystallinity in Fibrous Proteins by Thermal Analysis and Infrared Spectroscopy, Macromolecules 39 (2006) 6161–6170, https://doi.org/10.1021/ma0610109.
[59] A. Micsonai, É. Moussong, F. Wien, E. Boros, H. Vadászi, N. Murvai, Y.-H. Lee, T. Molnár, M. Réfrégiers, Y. Goto, Á. Tantos, J. Kardos, BeStSel: webserver for secondary structure and fold prediction for protein CD spectroscopy, Nucleic Acids Res. 50 (2022) W90–W98, https://doi.org/10.1093/nar/gkac345.
[60] A. Micsonai, É. Moussong, N. Murvai, Á. Tantos, O. Tőke, M. Réfrégiers, F. Wien, J. Kardos, Disordered–Ordered Protein Binary Classification by Circular Dichroism Spectroscopy, Front. Mol. Biosci. 9 (2022) 863141, https://doi.org/10.3389/fmolb.2022.863141.
[61] D. Tatini, M. Raudino, M. Ambrosi, E. Carretti, I. Davidovich, Y. Talmon, B. W. Ninham, P. Lo Nostro, Physicochemical characterization of green sodium oleate-based formulations. Part 1. Structure and rheology, J. Colloid Interface Sci. 590 (2021) 238–248, https://doi.org/10.1016/j.jcis.2021.01.040.
[62] K. Yuzu, N. Yamamoto, M. Noji, M. So, Y. Goto, T. Iwasaki, M. Tsubaki, E. Chatani, Multistep Changes in Amyloid Structure Induced by Cross-Seeding on a Rugged Energy Landscape, Biophys. J. 120 (2021) 284–295, https://doi.org/10.1016/j.bpj.2020.12.005.
[63] T. Hiramatsu, N. Yamamoto, S. Ha, Y. Masuda, M. Yasuda, M. Ishigaki, K. Yuzu, Y. Ozaki, E. Chatani, Iodine staining as a useful probe for distinguishing insulin amyloid polymorphs, Sci. Rep. 10 (2020) 16741, https://doi.org/10.1038/s41598-020-73460-y.
[64] M. Biancalana, S. Koide, Molecular mechanism of Thioflavin-T binding to amyloid fibrils, Biochim. Biophys. Acta BBA - Proteins Proteom. 1804 (2010) 1405–1412, https://doi.org/10.1016/j.bbapap.2010.04.001.
[65] A. Daina, O. Michielin, V. Zoete, iLOGP: A Simple, Robust, and Efficient Description of *n* -Octanol/Water Partition Coefficient for Drug Design Using the GB/SA Approach, J. Chem. Inf. Model. 54 (2014) 3284–3301, https://doi.org/10.1021/ci500467k.
[66] A. Daina, O. Michielin, V. Zoete, SwissADME: a free web tool to evaluate pharmacokinetics, drug-likeness and medicinal chemistry friendliness of small molecules, Sci. Rep. 7 (2017) 42717, https://doi.org/10.1038/srep42717.
[67] A.W.P. Fitzpatrick, G.T. Debelouchina, M.J. Bayro, D.K. Clare, M.A. Caporini, V. S. Bajaj, C.P. Jaroniec, L. Wang, V. Ladizhansky, S.A. Müller, C.E. MacPhee, C. A. Waudby, H.R. Mott, A. De Simone, T.P.J. Knowles, H.R. Saibil, M. Vendruscolo, E.V. Orlova, R.G. Griffin, C.M. Dobson, Atomic structure and hierarchical assembly of a cross-β amyloid fibril, Proc. Natl. Acad. Sci. 110 (2013) 5468–5473, https://doi.org/10.1073/pnas.1219476110.
[68] E. Chatani, K. Yuzu, Y. Ohhashi, Y. Goto, Current Understanding of the Structure, Stability and Dynamic Properties of Amyloid Fibrils, Int. J. Mol. Sci. 22 (2021) 4349, https://doi.org/10.3390/ijms22094349.
[69] Y. Kim, J.-H. Park, H. Lee, J.-M. Nam, How Do the Size, Charge and Shape of Nanoparticles Affect Amyloid β Aggregation on Brain Lipid Bilayer? Sci. Rep. 6 (2016) 19548 https://doi.org/10.1038/srep19548.
[70] P.N. Nirmalraj, J. List, S. Battacharya, G. Howe, L. Xu, D. Thompson, M. Mayer, Complete aggregation pathway of amyloid β (1-40) and (1-42) resolved on an atomically clean interface, Sci. Adv. 6 (2020) eaaz6014, https://doi.org/10.1126/sciadv.aaz6014.
[71] R. Liang, A. Khursheed, B. Tahirbegi, A.P. Torres-Flores, S. Qi, Y. Tian, H. Zhang, P. Szwedziak, V.A. Volkov, V.C. Darbari, J.H. Viles, Amyloid-β oligomers, curvilinear and annular assemblies, imaged by cryo-ET, cryo-EM, and AFM, Sci. Adv. 11 (2025) eadx9030, https://doi.org/10.1126/sciadv.adx9030.
[72] A. Dubnovitsky, A. Sandberg, M.M. Rahman, I. Benilova, C. Lendel, T. Härd, Amyloid-β Protofibrils: Size, Morphology and Synaptotoxicity of an Engineered Mimic, PLoS. ONE 8 (2013) e66101, https://doi.org/10.1371/journal.pone.0066101.
[73] R. Khurana, C. Ionescu-Zanetti, M. Pope, J. Li, L. Nielson, M. Ramírez-Alvarado, L. Regan, A.L. Fink, S.A. Carter, A General Model for Amyloid Fibril Assembly Based on Morphological Studies Using Atomic Force Microscopy, Biophys. J. 85 (2003) 1135–1144, https://doi.org/10.1016/S0006-3495(03)74550-0.
[74] C. Sachse, M. Fändrich, N. Grigorieff, Paired β-sheet structure of an Aβ(1-40) amyloid fibril revealed by electron microscopy, Proc. Natl. Acad. Sci. 105 (2008) 7462–7466, https://doi.org/10.1073/pnas.0712290105.
[75] A. Miller, S. Chia, E. Klimont, T.P.J. Knowles, M. Vendruscolo, F.S. Ruggeri, Maturation-dependent changes in the size, structure and seeding capacity of Aβ42 amyloid fibrils, Commun. Biol. 7 (2024) 153, https://doi.org/10.1038/s42003-024-05858-7.
[76] S. Yang, Q. Zhang, H. Yang, H. Shi, A. Dong, L. Wang, S. Yu, Progress in infrared spectroscopy as an efficient tool for predicting protein secondary structure, Int. J.

Biol. Macromol. 206 (2022) 175–187, https://doi.org/10.1016/j.ijbiomac.2022.02.104.
[77] M.R. Hilaire, B. Ding, D. Mukherjee, J. Chen, F. Gai, Possible Existence of α-Sheets in the Amyloid Fibrils Formed by a $TTR_{105–115}$ Mutant, J. Am. Chem. Soc. 140 (2018) 629–635, https://doi.org/10.1021/jacs.7b09262.
[78] I. Amenabar, S. Poly, W. Nuansing, E.H. Hubrich, A.A. Govyadinov, F. Huth, R. Krutokhvostov, L. Zhang, M. Knez, J. Heberle, A.M. Bittner, R. Hillenbrand, Structural analysis and mapping of individual protein complexes by infrared nanospectroscopy, Nat. Commun. 4 (2013) 2890, https://doi.org/10.1038/ncomms3890.
[79] R. Sarroukh, E. Goormaghtigh, J.-M. Ruysschaert, V. Raussens, ATR-FTIR: A "rejuvenated" tool to investigate amyloid proteins, Biochim. Biophys. Acta BBA - Biomembr. 1828 (2013) 2328–2338, https://doi.org/10.1016/j.bbamem.2013.04.012.
[80] E. Cerf, A. Gustot, E. Goormaghtigh, J.-M. Ruysschaert, V. Raussens, High ability of apolipoprotein E4 to stabilize amyloid-β peptide oligomers, the pathological entities responsible for Alzheimer's disease, FASEB J. 25 (2011) 1585–1595, https://doi.org/10.1096/fj.10-175976.
[81] M. Grechko, M.T. Zanni, Quantification of transition dipole strengths using 1D and 2D spectroscopy for the identification of molecular structures via exciton delocalization: Application to α-helices, J. Chem. Phys. 137 (2012) 184202, https://doi.org/10.1063/1.4764861.
[82] A. Barth, Infrared spectroscopy of proteins, Biochim. Biophys. Acta BBA - Bioenerg. 1767 (2007) 1073–1101, https://doi.org/10.1016/j.bbabio.2007.06.004.
[83] A.Ya Malkin, S.R. Derkach, V.G. Kulichikhin, Rheology of Gels and Yielding Liquids, Gels 9 (2023) 715, https://doi.org/10.3390/gels9090715.
[84] S.H. Hiew, H. Mohanram, L. Ning, J. Guo, A. Sánchez-Ferrer, X. Shi, K. Pervushin, Y. Mu, R. Mezzenga, A. Miserez, A Short Peptide Hydrogel with High Stiffness Induced by 3_{10} -Helices to β-Sheet Transition in Water, Adv. Sci. 6 (2019) 1901173, https://doi.org/10.1002/advs.201901173.
[85] Md.M.H. Rumon, A.A. Akib, F. Sultana, Md Moniruzzaman, M.S. Niloy, M. S. Shakil, C.K. Roy, Self-Healing Hydrogels: Development, Biomedical Applications, and Challenges, Polymers 14 (2022) 4539, https://doi.org/10.3390/polym14214539.
[86] J. Rodon Fores, M. Criado-Gonzalez, A. Chaumont, A. Carvalho, C. Blanck, M. Schmutz, F. Boulmedais, P. Schaaf, L. Jierry, Autonomous Growth of a Spatially Localized Supramolecular Hydrogel with Autocatalytic Ability, Angew. Chem. Int. Ed. 59 (2020) 14558–14563, https://doi.org/10.1002/anie.202005377.
[87] L. Medda, B. Barse, F. Cugia, M. Boström, D.F. Parsons, B.W. Ninham, M. Monduzzi, A. Salis, Hofmeister Challenges: Ion Binding and Charge of the BSA Protein as Explicit Examples, Langmuir 28 (2012) 16355–16363, https://doi.org/10.1021/la3035984.
[88] K.B. Rembert, J. Paterová, J. Heyda, C. Hilty, P. Jungwirth, P.S. Cremer, Molecular Mechanisms of Ion-Specific Effects on Proteins, J. Am. Chem. Soc. 134 (2012) 10039–10046, https://doi.org/10.1021/ja301297g.
[89] J. Paterová, K.B. Rembert, J. Heyda, Y. Kurra, H.I. Okur, W.R. Liu, C. Hilty, P. S. Cremer, P. Jungwirth, Reversal of the Hofmeister Series: Specific Ion Effects on Peptides, J. Phys. Chem. B 117 (2013) 8150–8158, https://doi.org/10.1021/jp405683s.
[90] O.A. Francisco, C.J. Clark, H.M. Glor, M. Khajehpour, Do soft anions promote protein denaturation through binding interactions? A case study using ribonuclease A, RSC Adv. 9 (2019) 3416–3428, https://doi.org/10.1039/C8RA10303H.
[91] B.A. Bauer, S. Ou, S. Patel, Role of spatial ionic distribution on the energetics of hydrophobic assembly and properties of the water/hydrophobe interface, Phys. Chem. Chem. Phys. 14 (2012) 1892, https://doi.org/10.1039/c1cp20839j.
[92] D. Corinti, B. Gregori, L. Guidoni, D. Scuderi, T.B. McMahon, B. Chiavarino, S. Fornarini, M.E. Crestoni, Complexation of halide ions to tyrosine: role of non-covalent interactions evidenced by IRMPD spectroscopy, Phys. Chem. Chem. Phys. 20 (2018) 4429–4441, https://doi.org/10.1039/C7CP06657K.
[93] J. Lim, S. Chin, A. Miserez, K. Xue, K. Pervushin, Trifluoroacetic Acid as a Molecular Probe for the Dense Phase in Liquid–Liquid Phase-Separating Peptide Systems, Anal. Chem. 97 (2025) 166–174, https://doi.org/10.1021/acs.analchem.4c03444.
[94] M. Acar, D. Tatini, B.W. Ninham, P. Lo Nostro, The Role of Polarizability in Isoelectronic Ions: The Case of Pseudohalides, Molecules 30 (2025) 323, https://doi.org/10.3390/molecules30020323.
[95] A. Iscen, G.C. Schatz, Hofmeister Effects on Peptide Amphiphile Nanofiber Self-Assembly, J. Phys. Chem. B 123 (2019) 7006–7013, https://doi.org/10.1021/acs.jpcb.9b05532.